

Location of the Antarctic Polar Front from AMSR-E Satellite Sea Surface Temperature Measurements

SHENFU DONG, JANET SPRINTALL, AND SARAH T. GILLE

Scripps Institution of Oceanography, University of California, San Diego, La Jolla, California

(Manuscript received 12 December 2005, in final form 5 May 2006)

ABSTRACT

The location of the Southern Ocean polar front (PF) is mapped from the first 3 yr of remotely sensed Advanced Microwave Scanning Radiometer for the Earth Observing System (AMSR-E) sea surface temperature (SST) measurements. In agreement with previous studies, the mean path of the Antarctic PF and its standard deviation are strongly influenced by bottom topography. However, the mean PF path diverges slightly from previous studies in several regions where there is high mesoscale variability. Although the SST and SST gradient at the PF show spatially coherent seasonal variations, with the highest temperature and the lowest temperature gradient during summer, the seasonal variations in the location of the PF are not spatially coherent. The temporal mean SST at the PF corresponds well to the mean PF path: the temperature is high in the Atlantic and Indian Ocean sections and is low in the Pacific Ocean section where the PF has a more southerly position. The relationship of the wind field with the Antarctic PF location and proxies for the zonal and meridional PF transports are examined statistically. Coherence analysis suggests that the zonal wind stress accelerates the zonal transport of the PF. The analysis presented herein also suggests that the meridional shifts of the Antarctic PF path correspond to the meridional shifts of the wind field.

1. Introduction

The Southern Ocean is distinguished from other oceans by the fact that it is the only oceanic region that circles the globe without being blocked by land. It experiences the strongest surface wind of any global open-ocean area. The main feature of the Southern Ocean is the strong eastward flow in the zonally connected Antarctic Circumpolar Current (ACC). The ACC connects the major world oceans and redistributes oceanic properties, such as heat, salt, and nutrients. The ACC consists of three major circumpolar fronts, which are, from north to south, the sub-Antarctic front (SAF), the Antarctic polar front (PF), and the southern Antarctic circumpolar front (SACCF). The fronts separate distinct surface water masses and are associated with strong currents and strong lateral gradients in temperature, salinity, and biological productivity (Nowlin et al. 1977; Boyd et al. 1995; Pollard et al. 1995, 2002;

Moore et al. 1999b; Moore and Abbott 2000, 2002; Barth et al. 2001).

The frontal structure in the ACC is complex, with the fronts splitting into multiple filaments or merging to form one single front (Read et al. 1995; Belkin and Gordon 1996; Sparrow et al. 1996; Holliday and Read 1997; Moore et al. 1999a; Sokolov and Rintoul 2002). The determination of the correct frontal position is important for studies of eddy-mean flow interaction (Hughes and Ash 2001), since slight shifts in frontal position can reverse the eddy-mean flow relationship. Previous studies (Botnikov 1963; Lutjeharms and Valentine 1984; Moore et al. 1997, 1999a) suggested that the Antarctic PF has both surface and subsurface expressions. The climatological mean surface and subsurface locations of the Antarctic PF have been examined in a number of studies (Orsi et al. 1995; Belkin and Gordon 1996; Moore et al. 1999a; Gille 1994, 1999), which are in relatively good agreement. Some of these studies (e.g., Gille 1994, 1999; Moore et al. 1999a) have also examined the time-varying PF locations on a global scale. However, the spatial and temporal resolutions of the altimetric sea surface height (SSH) measurements used by Gille (1994) and Gille (1999) were comparatively coarse. Moore et al. (1999a) determined the sur-

Corresponding author address: Shenfu Dong, Scripps Institution of Oceanography, UCSD, Mail Code 0230, 9500 Gilman Dr., La Jolla, CA 92093-0230.
E-mail: shdong@ucsd.edu

face PF location from weekly composites of the daily images of SST measured from infrared sensors. While the spatial resolution of the SST maps was high (9 km), the infrared SST measurements that Moore et al. (1999a) used are strongly influenced by water vapor and cloud cover, and about 45% of the data during their study period were missing. Moore et al. (1999a) suggested that both the Antarctic PF path and its properties show seasonal variability, although they also mentioned that the cloud cover itself has seasonal variability. Cloud cover leaves a number of open questions in the Moore et al. (1999a) analysis, suggesting that the topic merits revisiting using a dataset that is unimpeded by clouds.

The recently launched Advanced Microwave Scanning Radiometer for the Earth Observing System (AMSR-E) now provides global all-weather SST measurements. The AMSR-E microwave radiometer measurements are the first data to show SSTs for the entire Southern Ocean with twice-daily temporal resolution. With its cloud-penetrating ability, AMSR-E provides a unique dataset to determine the Antarctic PF location and to examine its spatial and temporal variations. Comparison of the PF from AMSR-E SST maps with that based on infrared SSTs can provide a measure of the effectiveness of infrared SSTs in determining the PF location and an evaluation of the influence of the seasonally biased cloud cover on the Antarctic PF path variability.

Many studies (Deacon 1937; Gordon et al. 1978; Chelton et al. 1990; Gille 1994; Moore et al. 1999a) have suggested that topography plays an important role in the Antarctic PF path and its variability. Analyses of both hydrographic data (Gordon et al. 1978) and satellite altimeter measurements (Chelton et al. 1990; Gille 1994) indicated that the fronts are steered by bottom topography. Moore et al. (1999a) argued that the bottom topography and corresponding planetary potential vorticity field (f/H) strongly influence the variability of the location and dynamics of the Antarctic PF, where f is the planetary vorticity and H is ocean depth.

The dynamics of the ACC have been a subject of debate mainly because of the presence of uninterrupted potential vorticity contours around the globe, which means free, unforced flow is possible. What determines the ACC transport? Several hypotheses have been proposed. Munk and Palmén (1951) suggested that the ACC transport should be directly proportional to wind stress, which is balanced by topographic form stress due to pressure gradients across ocean ridges. In contrast, Hidaka and Tsuchiya (1953), Stommel (1957), and Warren et al. (1996) suggested that the ACC transport is controlled by a Sverdrup balance. Thus, the strong

wind stress curl in the Southern Ocean is the primary forcing for the ACC. Fofonoff (1955) and Barcilon (1967) studied the buoyancy forcing in driving the ACC and argued that the buoyancy loss would enhance the ACC transport. Johnson and Bryden (1989) and Straub (1993) have suggested that the ACC transport is controlled by the angular momentum budget. Tansley and Marshall (2001) concluded that the ACC transport is determined by an integral momentum balance with a combined forcing from wind, buoyancy, eddy fluxes, and friction. Modeling studies (Gnanadesikan and Hallberg 2000; Gent et al. 2001) suggested that neither Sverdrup balance nor the mean wind stress at the latitudes of Drake Passage determines the ACC transport, and the ACC transport can be altered by the transformation of dense water to light water in the Southern Ocean. Using the AMSR-E measurements, we will examine the possible response of the time-varying Antarctic PF transport to wind forcing in the Southern Ocean in a statistical sense.

In this study, we use the first 3 yr of the AMSR-E SST measurements to map the Antarctic PF locations and study the PF variability. The data used in this study and the technique used to determine the Antarctic PF location from the SST measurements are described in section 2, which also provides an evaluation of the technique using XBT observations along two Southern Ocean transects. Section 3 describes the mean PF path and the mean SST and SST gradient at the PF, and their temporal and spatial variations. The relationship between the Antarctic PF transport and wind are examined in section 4. The conclusions are given in section 5.

2. Data and method

a. AMSR-E SST

AMSR-E is a multichannel passive microwave radiometer that was launched on the National Aeronautics and Space Administration (NASA) *Aqua* satellite on 4 May 2002. The *Aqua* satellite is in a sun-synchronous polar orbit, so observations occur at the same local time each day with equator crossings at 1230 and 0130 LT. Southern Ocean crossings at 55°S are around 1500 and 0100 LT. AMSR-E measures a wide range of geophysical parameters, including SST, wind speed, columnar water vapor, and columnar cloud water. Three years (June 2002–June 2005) of daily and weekly SST observations from version-4 AMSR-E ocean products (obtained online at <http://www.ssmi.com>) are used in this study to determine the Antarctic PF location. Both daily and weekly AMSR-E data are on a 0.25° latitude × 0.25° longitude grid. An assessment of the accuracy of the AMSR-E SST measurements in the

Southern Ocean is given by Dong et al. (2006). They found that, when compared with Moderate Resolution Imaging Spectroradiometer (MODIS) and Reynolds optimal interpolation (OI) SSTs, AMSR-E SSTs have less bias relative to in situ observations and also have better temporal coverage.

b. Criteria to determine the surface expression of the Antarctic PF

Like many fronts, the surface Antarctic PF is characterized by strong gradients in oceanic properties. Moore et al. (1999a) used the strong SST gradient across the PF to determine its location from Advanced Very High Resolution Radiometer (AVHRR) maps. They defined a strong gradient as a temperature change of $\geq 1.35^{\circ}\text{C}$ over a distance of 45–65 km (depending on latitude and PF orientation) from weekly composites of the daily AVHRR SST maps with 9-km resolution. In this study, we tested several different methods to determine the PF location from AMSR-E SST measurements including the maximum SST gradient within a certain temperature range, the southern bound of the SST gradient above a certain limit, or a fixed isotherm. Like Moore et al. (1999a), we found that a criterion based on the southern bound of the SST gradient above a certain limit gives a more stable result, although we use a lower limit because of the relatively coarse resolution of the AMSR-E maps compared to the AVHRR data. The PF path is determined following three steps.

- 1) Instead of defining the temperature gradient as the largest gradient in four directions (N–S, E–W, NE–SW, NW–SE) as in Moore et al. (1999a), the SST gradient at each AMSR-E grid is computed as the absolute gradient, $|\nabla T| = \sqrt{(\partial T/\partial x)^2 + (\partial T/\partial y)^2}$.
- 2) At each longitude the Antarctic PF location is determined to be the southernmost location at which the SST gradient exceeds $1.5 \times 10^{-2}^{\circ}\text{C km}^{-1}$. Small patches (less than 3° longitude) of high SST gradient are removed to avoid incorrectly identifying eddies as the PF location.
- 3) The PF location and the SST at the PF from step 2 above occasionally show large difference at adjacent locations. In regions where the PF location and the SST at the PF differ from adjacent values by more than two standard deviations of the difference, the PF location is automatically corrected to the southern bound of the high SST gradient that is closest. This ensures the spatial and thermal continuity of the PF path. In this correction, we relax the SST gradient limit to $1 \times 10^{-2}^{\circ}\text{C km}^{-1}$.

In a few cases the Antarctic PF location cannot be determined using the above three steps because of a

weak SST gradient. In these cases we further relax the SST gradient limit to $0.8 \times 10^{-2}^{\circ}\text{C km}^{-1}$ in step 3, and locate the PF based on spatial and thermal continuity. Thus, a unique PF is designated at all longitudes. In regions with relatively low SST gradients, such as the southeast Pacific Ocean, the determination of the PF location will rely on the spatial and thermal continuity of the PF path (the third step in our technique). We will mainly present the results from weekly AMSR-E SST maps, which give more spatially continuous results. The daily SST maps have gaps between ground tracks that influence the continuity of the Antarctic PF path both in space and time. To examine the effect of the smoothness of the weekly SST field on the results, we compared the location of the PF from the weekly AMSR-E SST maps with that determined from the daily maps. The results from daily and weekly maps are consistent in terms of the spatial and temporal variability. We also examined the effect of errors in the AMSR-E SST measurements on the Antarctic PF. A Monte Carlo simulation was performed: random errors with a standard deviation of 0.3°C , based on the accuracy of the AMSR-E SST measurements, were added to the weekly SST maps, and the location of the PF was determined from these maps. The process was repeated 1000 times. The standard deviation of the mean PF path from each repeated process is small (~ 50 km) relative to the temporal variations of the PF path, indicating that our results are not strongly sensitive to errors in the AMSR-E SST measurements.

Figure 1 shows an example of the SST and the corresponding SST gradient from a weekly AMSR-E map. The PF determined using the above technique is indicated by the black curve, which departs from the 2°C isotherm. The 2°C isotherm is a good approximation of the northern limit of the subsurface minimum temperature, which is used traditionally to identify the subsurface PF (e.g., Botnikov 1963). Multiple filaments of the Antarctic PF have been found at several regions: Drake Passage (Sievers and Nowlin 1984), the southern Indian Ocean (Belkin and Gordon 1996; Sparrow et al. 1996; Holliday and Read 1997), the South Pacific (Read et al. 1995; Moore et al. 1999a), and south of Tasmania (Sokolov and Rintoul 2002). However, our technique only picks one location at each longitude. This uniqueness of the PF also means that we cannot resolve the meanders in the PF when the PF loops across the same longitude more than once.

c. Verification of the Antarctic PF criterion

To verify our technique for determining the location of the Antarctic PF, we apply the method to the in situ temperature measurements from high-resolution ex-

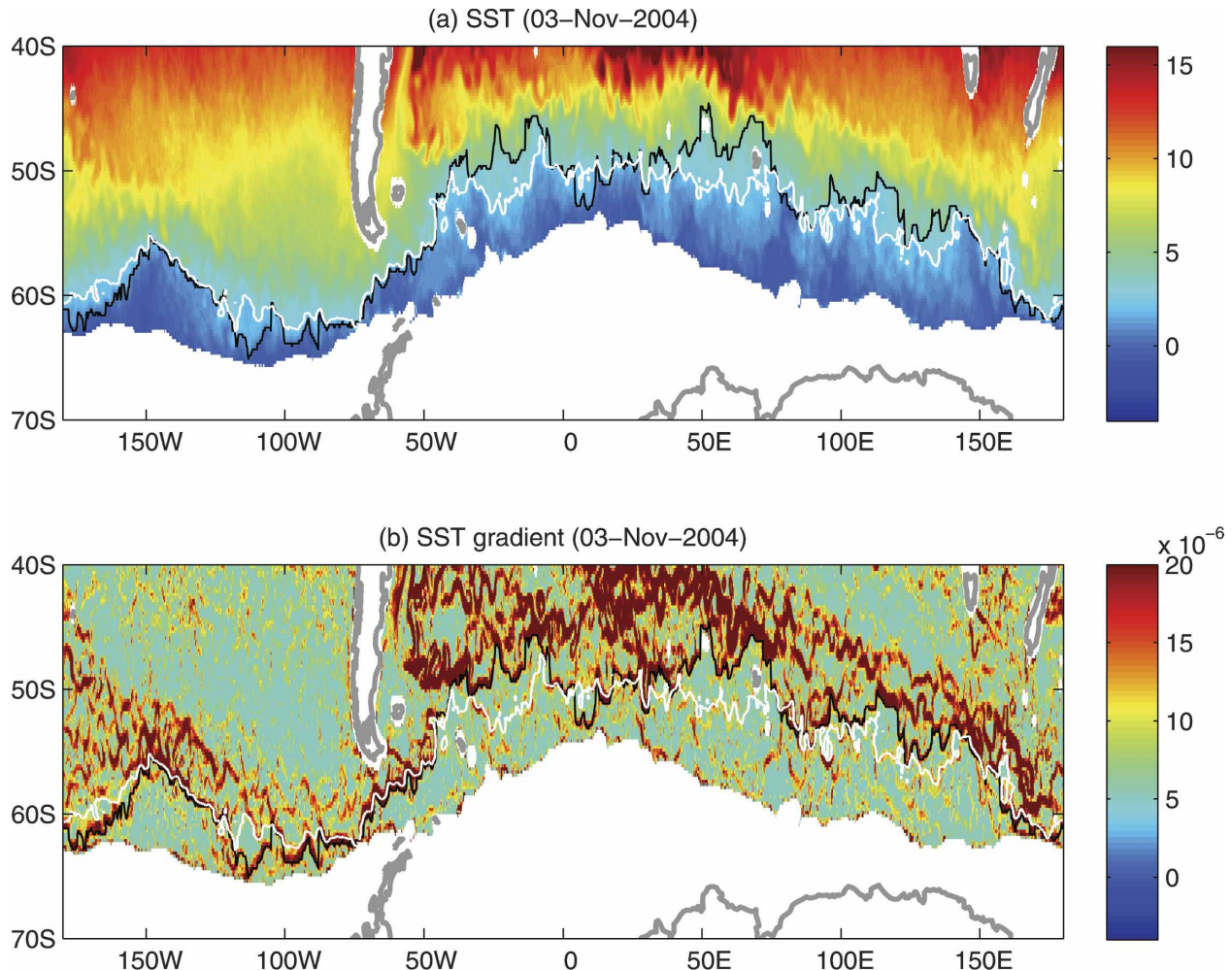


FIG. 1. (a) Example of the weekly AMSR-E SST map on 3 Nov 2004, and (b) the corresponding SST gradient. The black curve is the PF location, and the white curve is the 2°C isotherm.

pendable bathythermograph (XBT) profiles collected along two repeat lines, one across Drake Passage and the other extending between Hobart, Australia, and the French Antarctic base at Dumont d'Urville. Detailed descriptions of the XBT data can be found in Sprintall (2003) for Drake Passage and Rintoul et al. (1997) and Morrow et al. (2003) for south of Australia. There are 17 transects south of Australia during the AMSR-E period. All of the transects were carried out during summer (October–March). In Drake Passage, where the observations are year-round, there are 11 XBT transects available during summer and 10 XBT transects during winter. The northern extent of the 2°C isotherm at 200-m depth is used to determine the subsurface PF (Botnikov 1963). The surface PF locations determined from the XBT measurements at 4-m depth and those from AMSR-E SST measurements are compared with the subsurface PF locations. The compari-

son will not only give an assessment of the criteria used to determine the PF location in this study, but also show the differences between the surface and subsurface expressions of the PF.

To determine the Antarctic PF location from the daily AMSR-E fields and XBT SSTs, we first average the XBT SSTs along each transect to match the 0.25° grid resolution of the AMSR-E SST maps. The AMSR-E SSTs from daily gridded maps are then interpolated to the XBT locations. Figure 2 shows examples of the SST and SST gradient from both XBT and AMSR-E SSTs for the two transects, Drake Passage and south of Australia. The AMSR-E SST measurements show relatively good agreement with the XBT SST observations, with the main structures of the XBT SST captured well by the AMSR-E SST. Similarly, all the major peaks in the XBT SST gradient are shown in the AMSR-E SST gradient. Our technique consistently

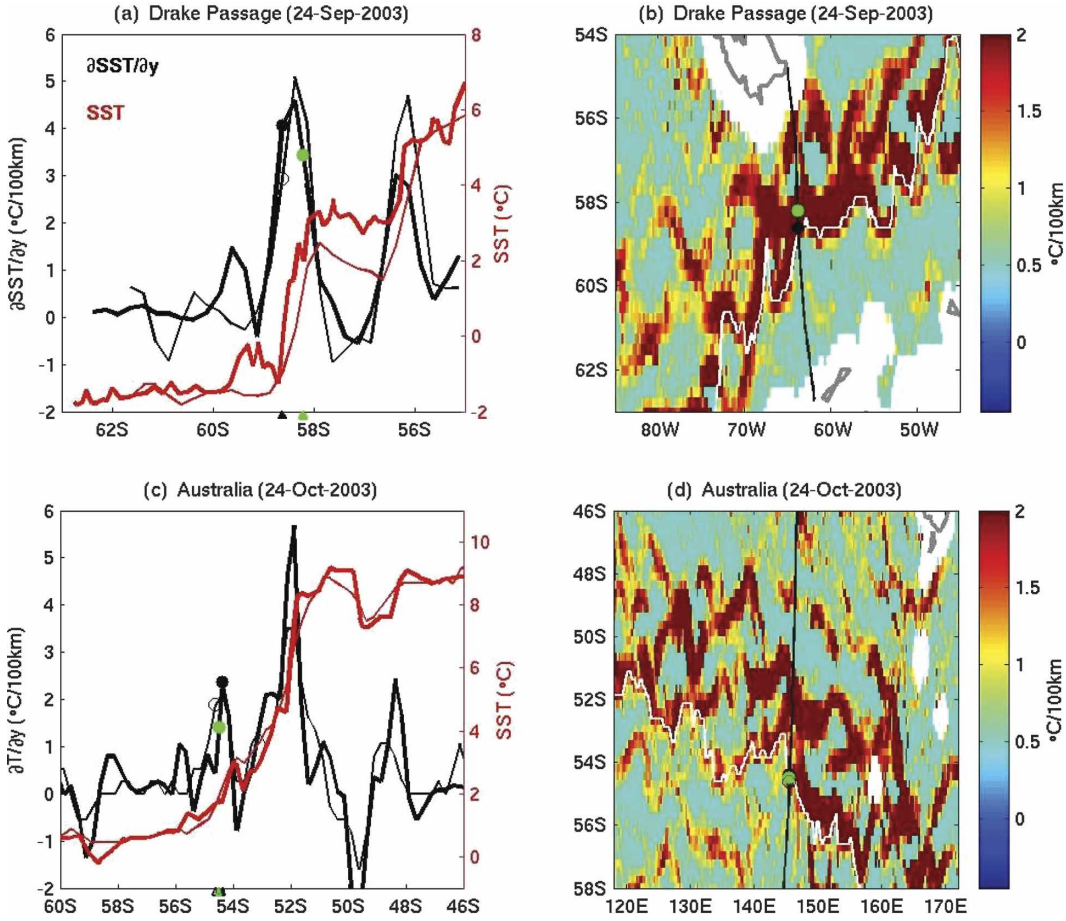


FIG. 2. (a) SST (red lines) and SST gradient (black) from XBT observations (thick lines) and AMSR-E measurements (thin) for a transect across Drake Passage in September 2003. (b) The corresponding spatial distribution of the SST gradient from AMSR-E, and the PF location (white line) from AMSR-E SST and the XBT transect (black line). The open circle is the surface PF location from AMSR-E and the dots are the surface (black) and subsurface (green) PF locations from XBT observations. (c), (d) Similar to (a) and (b) but for a transect south of Australia in October 2003.

picks out the same peak as the surface PF location from the AMSR-E and XBT observations. This peak is close to the subsurface PF location determined from the XBT temperature observations. In Drake Passage (Fig. 2a) the SST jumps from below -1° to above 3°C across the PF. The PF is between 58° and 59°S , identified by the strongest SST gradient ($\sim 5 \times 10^{-2}^{\circ}\text{C km}^{-1}$). The SAF can also be seen as the relatively smaller peak in SST gradient north of the PF at 56°S . For the transect south of Australia (Fig. 2c), the PF is identified as a relatively weak SST gradient ($\sim 2.5 \times 10^{-2}^{\circ}\text{C km}^{-1}$) at 54.5°S . The change in SST across the PF is less than 2°C . The strongest SST gradient at 52°S is the SAF. Figures 2b and 2d show the plan view of the SST gradient from the AMSR-E and the locations of the surface and subsurface PFs. The SST gradient in the Drake Passage is generally strong and has better zonal conti-

nuity in comparison with that south of Australia, where the PF may have multiple filaments (Belkin and Gordon 1996; Sokolov and Rintoul 2002).

Time series of the collocated surface and subsurface PF locations from in situ XBT temperature observations and the surface PF locations from daily and weekly AMSR-E SST maps are shown in Fig. 3. The temporal variations in the surface PF from both XBT and AMSR-E and the subsurface PF are consistent. The surface PF location tends to be south of the subsurface PF location, although the differences between the two are usually less than 1° latitude. The PF location from the weekly AMSR-E maps also captures the variability of the subsurface PF location. Overall, the comparison suggests that our method gives a reasonable PF location and can be applied to the AMSR-E SST maps.

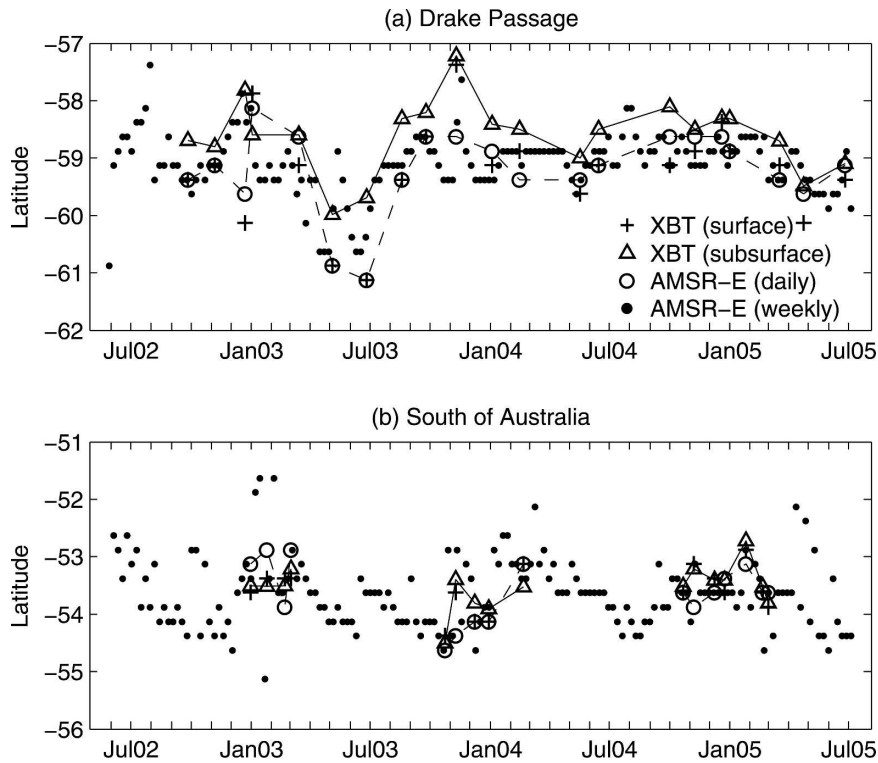


FIG. 3. Collocated subsurface PF location from XBT observations (triangle) and surface PF location from daily AMSR-E SST measurements (open circle) and XBT SSTs (plus sign) for the transects (a) near Drake Passage and (b) south of Australia. The dots are the time series of the surface PF location from the weekly AMSR-E SST maps at the mean longitude of the PF from the XBT profiles.

The year-round XBT observations from Drake Passage (Fig. 3a) indicate a seasonal cycle in the Antarctic PF locations. Over the 3-yr time series, the PF is farther to the south during austral winter and to the north during summer. Moore et al. (1999a) found that the global mean latitude of the Antarctic PF was farthest south in winter and at the northernmost position in fall; however, there was no discernible seasonal cycle across the Drake Passage. Sprintall (2003) did not find a seasonal cycle in the PF from the longer 7-yr XBT record along this transect. Thus, the apparent seasonal cycle that we find may be the result of the short duration of this study. The seasonal variations in the PF location south of Australia cannot be examined from the summer-only XBT observations. However, the PF locations from the weekly AMSR-E data can be used for a detailed examination of the seasonal variations, which will be performed in section 3.

3. Results

a. Mean Antarctic PF location

The mean PF paths from different studies (Orsi et al. 1995; Belkin and Gordon 1996; Moore et al. 1999a;

Gille 1999) are shown in Fig. 4a. Using historical hydrographic data, Orsi et al. (1995) defined the Antarctic PF as the position where the temperature minimum of the Antarctic Surface Water starts to descend northward. Belkin and Gordon (1996), also using historical hydrographic data, determined the PF as the northern extent of the subsurface minimum temperature layer bounded by the 2°C isotherm at 100–300-m depth. The PF path of Gille (1999) was determined from altimetric SSH measurements using a synthetic jet method (Gille 1994), designed to locate a surface geostrophic jet that is expected to coincide with the subsurface PF. Moore et al. (1999a) mapped the PF from remotely sensed infrared SST measurements based on a strong SST gradient at the front. Despite the differences in defining the PF, the mean PF path from each study shows relatively good agreement, particularly in the vicinity of strong topographic features, such as occur at the Agulhas Retroflection (15°–25°E), Kerguelen Plateau (75°–90°E), Pacific–Antarctic Ridge (150°–130°W), and Drake Passage (70°–50°W). Relatively large differences are seen in the southern Indian Ocean between 50° and 70°E, where the surface and subsurface PFs may differ (Sparrow et al. 1996) and the 2°C temperature mini-

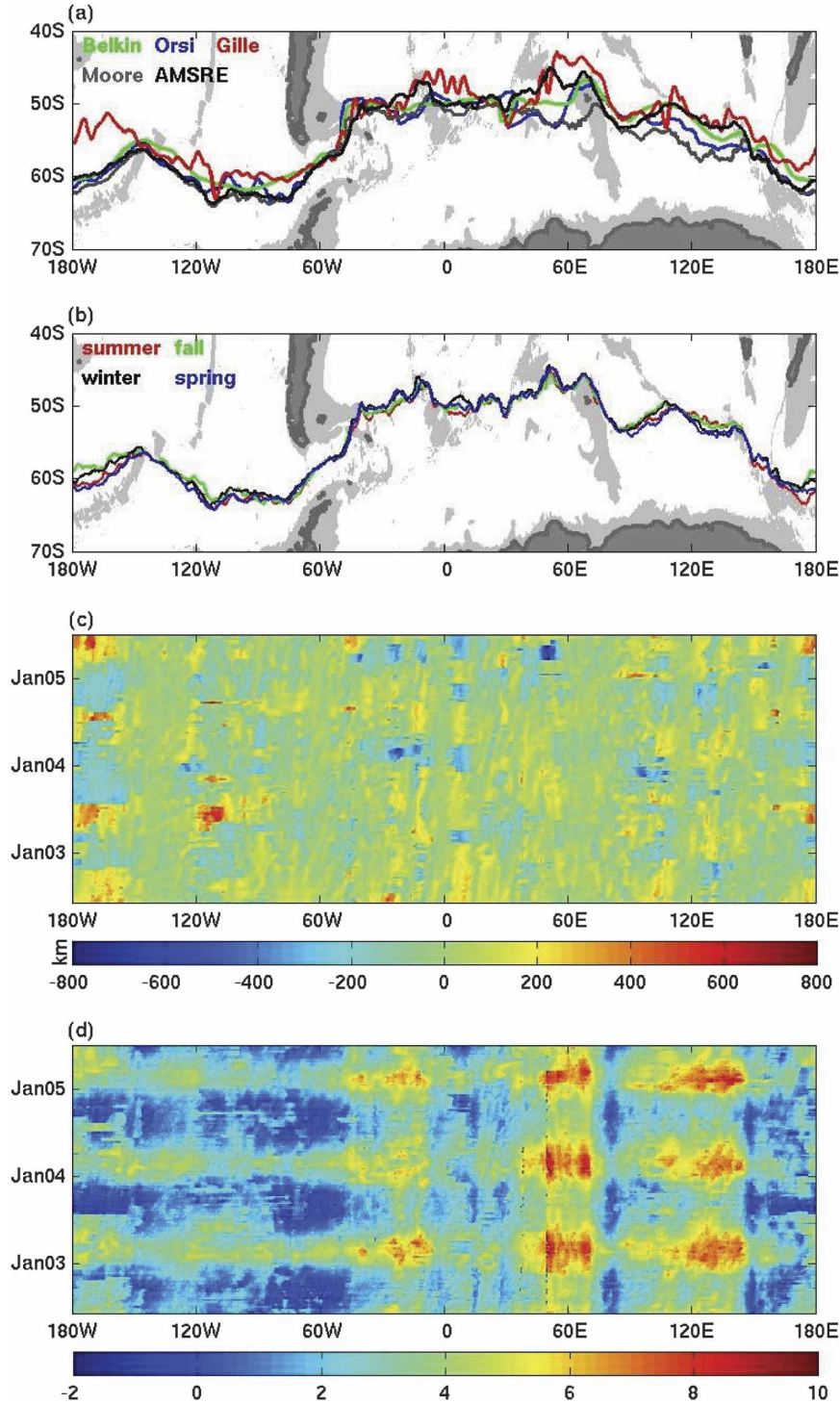


FIG. 4. (a) Mean PF paths from AMSR-E (black), Moore et al. (1999a) (gray), Orsi et al. (1995) (blue), Belkin and Gordon (1996) (green), and Gille (1999) (red). The light-shaded regions indicate where the bottom depth is shallower than 3000 m. (b) Seasonal-mean PF path for summer (red), autumn (green), winter (black), and spring (blue). Spatial distribution of (c) the anomalous location of the PF and (d) the SST at the PF.

mum that generally defines the subsurface PF may not be associated with an ACC jet (Park et al. 1993; Pollard et al. 2002).

The Antarctic PF path varies spatially in its mean position (Fig. 4a). The mean PF path is farther south in the South Pacific sector relative to the Atlantic Ocean and Indian Ocean sectors. The north–south range of the mean PF path is about 20° latitude, which is greater than the temporal variations at each location (Fig. 4c).

Like the PF criterion of Moore et al. (1999a), our criterion preferentially selects the southern boundary of the surface PF. The mean PF path from AMSR-E follows that from Moore et al. (1999a) over most regions. However, the two mean surface PF paths differ by about 2° – 8° latitude in some regions, such as 35° – 75° E, 100° – 140° E, and 25° – 5° W. The regions that show a large difference between our PF path and that of Moore et al. (1999a) coincide with the areas where the AVHRR data are heavily contaminated by cloud and so the PF was mapped infrequently over their 7-yr study period (Moore et al. 1999a, their Fig. 3). Those regions also coincide with where PF variability is strong (Fig. 5). In those regions our mean path agrees more closely with that of Gille (1999) and Belkin and Gordon (1996).

Previous studies of the Antarctic PF suggested that the surface expression is generally to the south of the subsurface expression (Botnikov 1963; Lutjeharms and Valentine 1984; Moore et al. 1999a). Indeed, the surface PF location from AMSR-E measurements tends to be south of the subsurface PF location from XBT observations (Fig. 3). Moore et al. (1999a) explained the difference of their mean PF from other studies as being due to the difference between surface and subsurface expressions of the PF. However, this does not explain the difference between the mean PF paths (Fig. 4a) in some areas where our surface PF path differs from that of Moore et al. (1999a) and others by a few degrees of latitude. The difference in mean PF paths could be attributed to a number of factors, including differences in the study period, the dataset (SSH, hydrographic data, SST), and the criteria (strong current, northern extent of the 2°C isotherm at 100–300-m depth, strong SST gradient) used to define the PF. The hydrographic data in the Southern Ocean are sparse in space and time, and so may not give as good a representation of the mean PF as those from the evenly distributed SSH and SST maps. The PF paths determined from SST maps were constrained by the continuity of the SST at the PF, whereas no thermal constraint was applied in determining the PF from SSH. Because of these differences, the surface geostrophic jet determined from the SSH (Gille 1999), the boundary of water masses

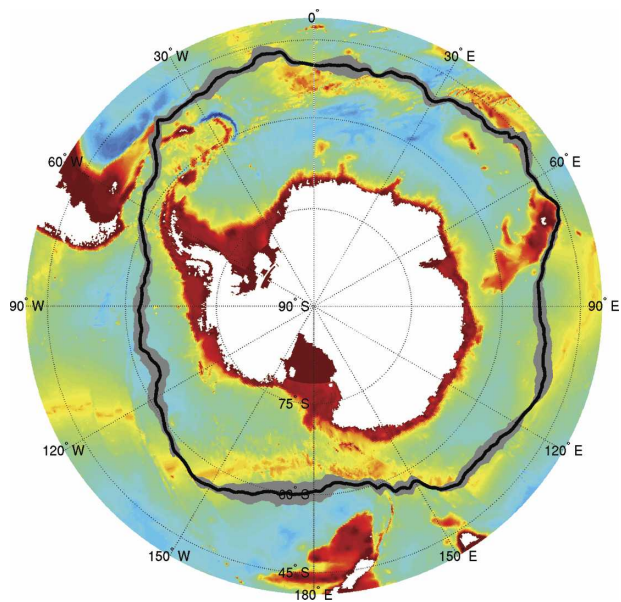


FIG. 5. Mean PF (black line) from the 3 yr of AMSR-E SST measurements and bottom topography (colors). The shaded area shows one std dev of the PF location.

marked by the 2°C isotherm at 200 m (Orsi et al. 1995; Belkin and Gordon 1996), and the location of strong SST gradient (Moore et al. 1999a) are likely to be displaced from each other. Another potential factor for the differences in the mean PF paths is the multiple-filament feature of the PF. For example, Holliday and Read (1997) found two surface PF paths south and east of South Africa (45° – 80° E). The northern branch is encountered around 45° – 50° S and the southern branch around 55° – 57° S at the Kerguelen Plateau. They pointed out that the temperature gradient of the southern branch was low. Our mean PF path is closer to their northern branch, whereas the mean PF path of Moore et al. (1999a) is closer to their southern branch. It is possible that the southern branch is too weak to be identified from our technique. Indeed, Moore et al. (1999a) found that the SST gradient across the front was weak and they often found two fronts in this region, of which they chose the southernmost (K. Moore 2006, personal communication). An alternative explanation is that the northern branch may lie in a cloudy region, so it cannot be detected from AVHRR data. This multiple filament feature may also explain differences in the mean PF paths in other regions, such as the southeast Pacific (120° – 80° W) noted by Read et al. (1995) and Moore et al. (1999a), and south of Australia (100° – 140° E) noted by Belkin and Gordon (1996) and Sokolov and Rintoul (2002).

Many studies (Gordon et al. 1978; Chelton et al. 1990; Gille 1994; Moore et al. 1999a) have found that

the fronts are closely steered by bottom topography. Figure 5 shows the mean PF path and its standard deviation (in cross-stream direction) as determined from AMSR-E measurements overlain on bottom topography. The topographic influence on the PF is apparent. The PF closely follows the topography in regions (65° – 85° E, 140° – 165° E, 15° W– 5° E, 150° – 140° W) with strong topographic features. In regions with steeply sloped bottom topography (65° – 85° E, 140° – 165° E, 150° – 130° W), the variability of the front is weak and the different mean PF paths (Fig. 4a) are in close agreement. Over the deep ocean basin regions (90° – 115° E, 175° – 160° W, and 120° – 80° W) with weak topographic constraint, the separation of the various mean PF paths (Fig. 4a) widens, and the PF experiences strong variability (Fig. 5).

To better examine the spatial distribution of the Antarctic PF variability and its relation with bottom topography, we show the standard deviation of the PF location (σ_{PF} , Fig. 6a), the bottom depth (Fig. 6c), and the bottom slope of the topography (Fig. 6d) at the mean location of the PF. The bottom slope is calculated in the cross-stream direction. Figures 6a, 6c, and 6d suggest that the spatial displacement of the PF path is largely constrained by the bottom topography. Large variability of the PF path (Fig. 6a) occurs near 105° E, 130° E, 175° W, 110° W, 25° W, and 15° W, where the ocean bottom is deep (Fig. 6c) and the bottom slope is weak (Fig. 6d) indicating weak topographic influence. Conversely, regions (65° – 80° E, 150° – 130° W, 65° – 55° W) with weak variability of the PF coincide with shallow and steeply sloped regions. The standard deviation of the PF location is up to 2° of latitude over the deep-basin regions and less than 0.5° of latitude in strong bottom topographically constrained regions. The correlations of the PF location variability with the bottom depth and the bottom slope are -0.25 and -0.32 , respectively. Both exceed the 95% significance level of 0.16, computed to account for the autocorrelation length scale of the PF path. The spatial displacement of the PF from AMSR-E maps is comparable to that of Moore et al. (1999a; Fig. 3c) in the Pacific and western Atlantic sectors (150° E– 30° W), whereas the displacement of Moore et al. (1999a) in the eastern Atlantic and Indian sectors was relatively high, which might be related to the high percentage of cloud cover over those regions. However, the weak variability of the PF was apparent from their study in regions with strong topographic features.

The temporally averaged SST gradient at the PF ($\partial T/\partial y$, Fig. 6b) shows good correspondence with σ_{PF} and ocean depth at the front: $\partial T/\partial y$ is weak over the regions with large variability of the PF path and greater

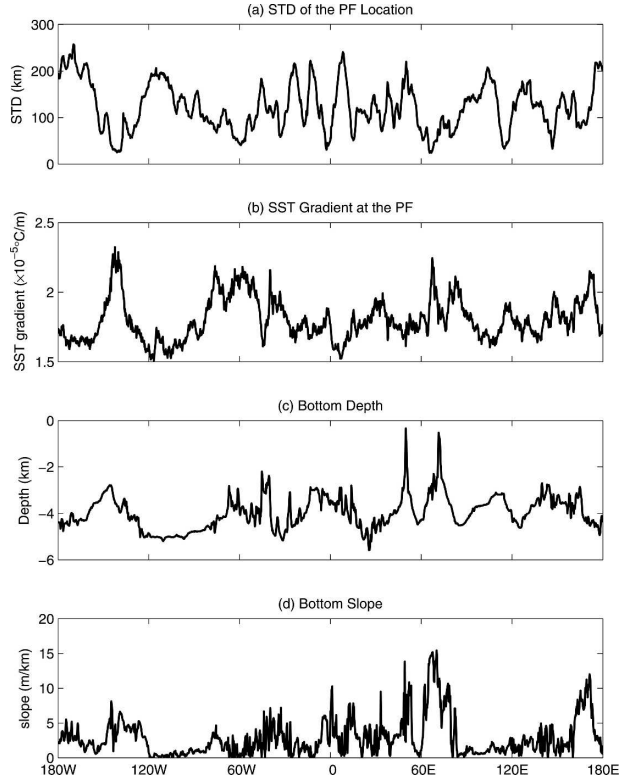


FIG. 6. Zonal distribution of the (a) std dev of the location of the PF, (b) temporally averaged absolute value of the SST gradient at the PF, (c) bottom depth at the mean location of the PF, and (d) absolute value of cross-stream bottom slope at the mean location of the PF.

ocean depth, and vice versa. $\partial T/\partial y$ is correlated with both bottom depth and slope; the correlation coefficients are 0.17 and 0.30, respectively. Both exceed the 95% significance level of 0.16. One possible explanation for the relationship is that $\partial T/\partial y$ from weekly SST maps is smeared out in places where the front meanders a lot on time scales shorter than 1 week. However, temporal mean $\partial T/\partial y$ from the daily AMSR-E maps shows a similar zonal distribution, suggesting that the low $\partial T/\partial y$ in regions with high σ_{PF} does not result from weekly averaging of the SST maps. The correspondence between σ_{PF} and $\partial T/\partial y$ may simply result from topographic effects on both the PF and SST gradient.

b. Spatial and temporal variability of the Antarctic PF path

The seasonal mean PF paths (Fig. 4b) do not show consistent spatial variation. The spatial distribution of seasonal variability of the PF location is similar to the spatial variability discussed in section 3a: low seasonal variability occurs in regions where topographic steering

is strong, and high seasonal variability occurs over the deep ocean basins where the bottom slope is weak. During summer (January–March), the PF has a more southerly position in most regions except in the eastern Pacific (140° – 120° W) and southwest of Australia (110° – 145° E). Over the Pacific (170° E– 120° W) and eastern Indian (90° – 140° E) sectors, the springtime (October–December) PF shifts to the south. The PF tends to move equatorward during winter except in the eastern Indian sector (90° – 140° E). However, overall the seasonal variability of the mean PF is relatively small in comparison with the differences in the mean PF paths from different studies (Figs. 4a and 4b).

The temporal variations of the Antarctic PF location (φ_{PF}) are shown more clearly in the global spatial distribution of the anomalous φ_{PF} (Fig. 4c). Although Fig. 4c shows a regular southward shift of the PF path in spring and summer in the western Pacific region (170° E– 160° W), other regions do not show persistent seasonal variations over the study period. Large temporal variations are found in regions (30° W– 10° E, 100° – 130° E, 170° E– 160° W, 120° – 110° W) with weak topographic constraints. The location of the PF in the western Pacific region (170° E– 160° W) appears to switch rapidly from a northerly position to a southerly position rather than gradually moving from north to south. Although the zonally averaged anomalous PF location (not shown) is small, the anomalies at any particular location can be larger than 5° of latitude.

c. SST and SST gradient at the Antarctic PF

The mean SST at the PF location (T_{PF} , Fig. 7a) varies with longitude from 1° to 6° C. The value of T_{PF} is high in the Atlantic and Indian sectors and is low in the Pacific sector. This zonal distribution of the mean SST corresponds well to the longitudinal variations in the mean PF path (Fig. 4a). The T_{PF} is high where the PF has an equatorward location and is low where the PF has a poleward location. The lowest temperature is seen just west of Drake Passage around 75° W. Low temperatures are also seen east of the Kerguelen Plateau (80° E) and south of Australia (150° E).

Unlike φ_{PF} (Fig. 4c), T_{PF} has a spatially coherent seasonal cycle (Fig. 4d) with amplitude shown in Fig. 7b. On average, the seasonal cycle explains 60% of the total variance in T_{PF} . The seasonal cycle of T_{PF} is strong at Drake Passage (60° – 40° W) and southwest of Australia (125° – 145° E) (Fig. 7b). The PF southwest of Africa (5° – 12° E) experiences the lowest seasonal variation in the SST. Like the PF path itself, the seasonal variations in T_{PF} (Fig. 7b) are relatively small in comparison with the spatial variability (Fig. 7a). However, the 3° C seasonal cycle (Fig. 7b) in T_{PF} is relatively high in com-

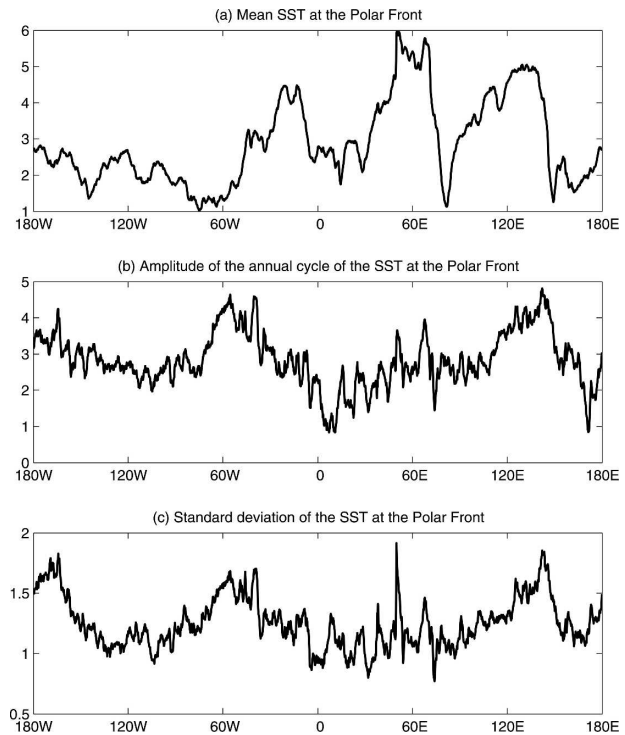


FIG. 7. Zonal distribution of the (a) temporal-mean SST at the PF location, (b) amplitude of the annual cycle of the SST at the PF, and (c) std deviation of the SST at the PF.

parison with its standard deviation (σ_T , Fig. 7c). The regions (180° – 160° W, 65° – 40° W, 125° – 150° E) where σ_T exceeds 1.5° C correspond well to the regions with high seasonal variability in T_{PF} (Fig. 7b), suggesting that the seasonal variability accounts for part of the spatial distribution of σ_T . In addition to undergoing a seasonal cycle, T_{PF} also varies in concert with meridional fluctuations of the φ_{PF} . This will be examined in the next section. The temporal variability of zonally averaged T_{PF} (Fig. 8) is dominated by the seasonal cycle, with high SST ($\sim 4.5^{\circ}$ C) during summer and low SST during winter ($\sim 1.5^{\circ}$ C). This seasonal cycle is consistent both in timing and amplitude with that from the XBT SSTs at the location of the subsurface PF in Drake Passage (not shown), although T_{PF} is more than 1° C colder than the SST at the location of the subsurface PF, because the surface PF is farther south (Fig. 3a). The mean T_{PF} is about 3° C, which is warmer than the 2° C criterion used traditionally to identify the subsurface PF location. If, as suggested in Drake Passage, the surface PF is farther south than the subsurface PF, we would expect that T_{PF} should be colder than 2° C. The warmer mean T_{PF} can be attributed to the warm T_{PF} in the Atlantic and Indian sectors (Fig. 3a) where our PF path is farther north than the PF paths from other studies (Fig. 4a).

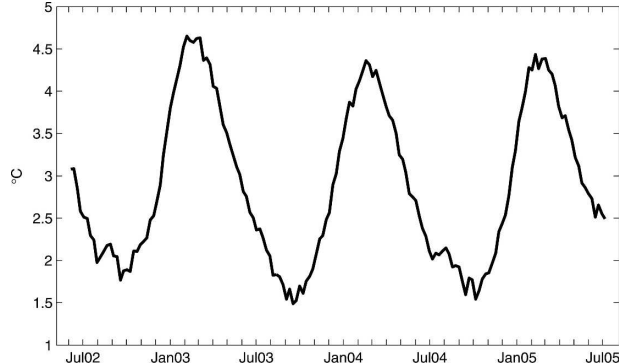


FIG. 8. Time series of zonally averaged SST at the location of the PF.

Previous studies (White and Tai 1995; Ferry et al. 2000) found that the SSH and the upper-ocean heat content agree well, suggesting that changes in upper-ocean thermal structure may reflect changes in the SSH. Examination of the mean maps of SSH and SST shows that gradients of the SSH and SST have similar spatial structure: high SST gradients coincide with high SSH gradients. Thus, the SST gradient at the Antarctic PF ($\partial T/\partial y$) can be thought of as a proxy for the zonal velocity of the PF. The zonally averaged $\partial T/\partial y$ (Fig. 9) clearly shows the seasonal cycle: $\partial T/\partial y$ is high during winter/spring and low during summer/autumn, which is consistent with the results of Moore et al. (1999a). This seasonal cycle is spatially coherent (not shown). The mean $\partial T/\partial y$ is about $1.8 \times 10^{-5} \text{ }^{\circ}\text{C m}^{-1}$ with a seasonal amplitude of $0.2 \times 10^{-5} \text{ }^{\circ}\text{C m}^{-1}$. The seasonal amplitude only explains 8% of the total variance in $\partial T/\partial y$ in the global average. In the Pacific sector the seasonal cycle is relatively strong and explains 20% of the total variance, suggesting that the velocity of the PF experiences relatively large seasonal variability in the Pacific sector. In the Atlantic and Indian sectors, seasonal variability only explains 5% of the total variance. This weak seasonal variability in $\partial T/\partial y$ may be related to the weak seasonal cycle in the wind field, which will be discussed in the next section.

4. Discussion

Both T_{PF} and φ_{PF} change spatially and temporally. Zonal variations in the temporal mean T_{PF} (Fig. 7a) covary with zonal variations in mean φ_{PF} (Fig. 4a). Temporal variations in T_{PF} can be attributed to two factors: 1) if the Antarctic PF path were invariant, then variations in T_{PF} would be due to the temporal variations in the SST field; 2) alternatively, if the SST field were invariant, then variations in T_{PF} would come from the temporal variations in φ_{PF} . Variations in T_{PF} are

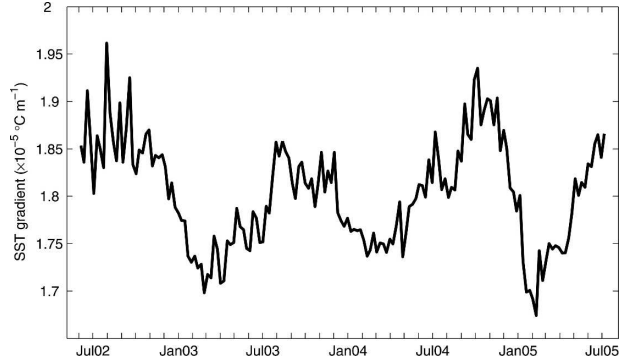


FIG. 9. Time series of the zonally averaged SST gradient at the location of the PF.

dominated by the spatially coherent seasonal cycle, while φ_{PF} does not show a coherent seasonal cycle. Our analysis shows that more than 80% of the seasonal cycle in T_{PF} can be explained by the seasonal cycle in SST, while only 10% of the T_{PF} seasonal cycle can be explained by the seasonal fluctuations in φ_{PF} . Here, we denote variables that have had a seasonal cycle removed with a prime, we find that φ'_{PF} and T'_{PF} have a correlation coefficient of 0.74, exceeding the 95% significance level of 0.15. This suggests that a negative T'_{PF} corresponds to a southward shift of the PF path. If we assume that T'_{PF} is due exclusively to the variations in φ'_{PF} , then we would expect that T'_{PF} should equal the product of φ'_{PF} and the meridional SST gradient ($\varphi'_{\text{PF}} \partial T / \partial y$). We computed this product using either a zonally and temporally varying or a constant SST gradient but found that the difference between the two products was small, suggesting that variations in $\varphi'_{\text{PF}} \partial T / \partial y$ are controlled by φ'_{PF} . Although the correlation between T'_{PF} and $\varphi'_{\text{PF}} \partial T / \partial y$ is high (~0.7), the magnitude of T'_{PF} is less than one-half that of $\varphi'_{\text{PF}} \partial T / \partial y$. The relatively weak T'_{PF} in comparison with the $\varphi'_{\text{PF}} \partial T / \partial y$ suggests that the displacements of the PF move the temperature field, which can also be seen from the correspondence between the standard deviation of T'_{PF} and that of the φ'_{PF} (Fig. 10).

The SST variations along the Antarctic PF path are consistent with those of Sun and Watts (2002) who found that the ACC warms in the South Atlantic and Indian Oceans (equatorward segments) and cools in the South Pacific (poleward segments). Sun and Watts (2002) suggested that the mean flow of the ACC transports heat from warm subtropical regions to cold subpolar regions. O'Neill et al. (2003) investigated the coupling between the near-surface wind field and the underlying SST field over the Southern Ocean and found that the wind stress curl and divergence are linearly related to the crosswind and downwind components of

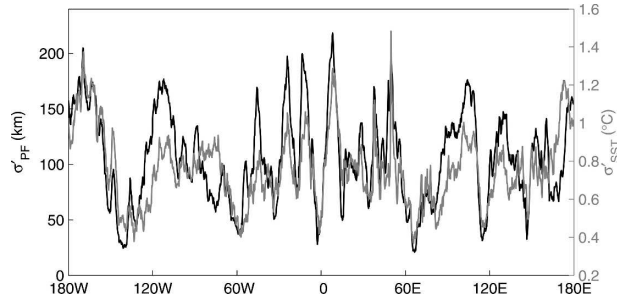


FIG. 10. Std deviation of the PF location (black) and the SST at the PF (gray). The seasonal cycle has been removed before computing the std dev.

the SST gradient, respectively. The SST field not only responds to meridional shifts of the fronts, it should also change with variations in the heat transport of the ACC, which is mostly accomplished by its major fronts (the SAF, PF, and SACC). The response of winds to SST may feed back into the ocean and modify the ocean current system. Thus, the variability of the strength and location of the fronts are important to the coupling of winds and upper-ocean processes.

The detailed time series of φ_{PF} and $\partial T/\partial y$ provided by AMSR-E allow us to probe the mechanism governing PF variations. Previous studies (Baker 1982; Warren et al. 1996; Wearne and Baker 1980, Peterson 1988, Hughes et al. 1999, Gille et al. 2001) suggest that the ACC is strongly wind forced. These studies were mostly based on localized observations with coarse temporal sampling. Here, we examine the response of the variability of the PF properties to wind, using surface PF properties from continuous AMSR-E measurements and wind fields from the Center for Ocean–Atmospheric Prediction Studies (COAPS). The COAPS gridded pseudo-stress fields are objectively mapped from Quick Scatterometer (QuikSCAT) measurements onto a $1^\circ \times 1^\circ$ grid (Pegion et al. 2000). We convert the 6-hourly COAPS fields to wind stress using the drag coefficient from Yelland and Taylor (1996), and average to produce the daily wind stress and wind stress curl.

The SST gradient at the Antarctic PF ($\partial T/\partial y$) and the time derivative of the PF location ($\partial \varphi_{\text{PF}}/\partial t$) are used as indices for the zonal (u) and meridional (v) ACC transport in the PF, respectively. Coherence analysis techniques are used to examine their relationship with the wind stress and wind stress curl, which are averaged in a 5° latitude band centered at the time-varying PF location at each longitude. Coherence analysis allows us to examine both the correlation and phase lag between the wind and PF transport as a function of frequency. Full time series at each longitude are Fourier transformed and results are zonally averaged to increase the

degrees of freedom for the coherence and phase calculations.

The zonal nature of the ACC suggests that we first need to understand the zonal momentum balance in order to understand the mechanisms governing the Antarctic PF variations. Studies based on bottom pressure data (e.g., Peterson 1988; Gille et al. 2001) have suggested that changes in wind stress should accelerate and decelerate ocean transport:

$$\frac{\partial u}{\partial t} = \tau^x.$$

This relationship implies that u and τ^x should be coherent with a 90° phase lag. To examine their relationship, we “prewhiten” the oceanic record u , by employing its tendency $\partial u/\partial t$, because ocean variables tend to be “red,” but we keep the atmospheric record τ^x , as atmospheric variables tend to be “white.” Prewhitening reduces the bias of the poorly resolved low-frequency components of time series and improves the reliability of the spectral analysis (Emery and Thomson 2001). The spectrum of u is flattened through prewhitening, thus making the examination of weak spectral components more effective. Although the coherence (Fig. 11a) between the zonal wind stress (τ^x) and $\partial u/\partial t$ is not high, except near the annual and semiannual frequencies, it is statistically significant at the 95% level in over 70% of the resolved frequencies. The phase between τ^x and $\partial u/\partial t$ (Fig. 11b) is typically near zero, but with a slight shift to the negative phase, more clearly shown in the histogram of the phase lag (Fig. 11c). The single peak in phase lag suggests that the zonal wind stress accelerates the zonal PF transport ($\partial u/\partial t \propto \tau^x$), and the negative phase lag suggests that the zonal wind stress slightly leads the zonal PF transport. This contrasts with the study of O’Neill et al. (2005) who found that perturbations in the SST gradient lead to perturbations in the wind field. The different result could be due to different air–sea interactions over different spatial scales. O’Neill et al. (2005) focused on the short-scale processes, whereas our results are based on zonal averages. The low coherence indicates that other mechanisms, such as baroclinic instability and bottom friction, are possibly important in determining the PF transport. Another scenario corresponding to the relationship between τ^x and $\partial T/\partial y$ is that the wind-forced upwelling and/or northward Ekman flux of light water strengthens the meridional SST gradient (Gnanadesikan and Hallberg 2000). Drawing on the results for the zonal momentum balance, we might imagine that changes in meridional wind stress (τ^y) accelerate meridional ocean transport. However, neither the meridional transport of

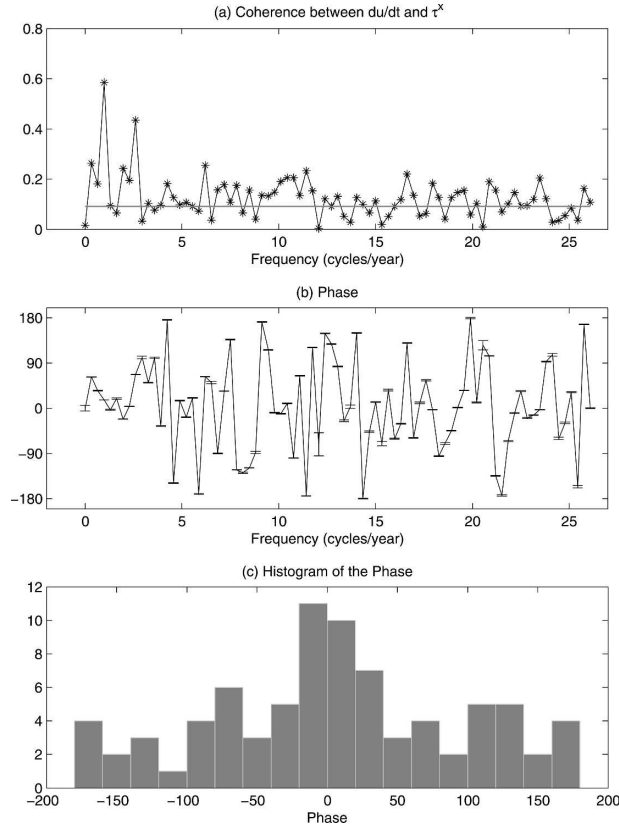


FIG. 11. (a) Coherence between the zonal wind stress and time derivative of the SST gradient at the PF (95% significance level given by the gray line) and (b) the corresponding phase. (c) Histogram of the phase.

the PF nor its tendency shows a statistically significant relationship with τ^y , implying either that they are unrelated or that our data do not capture the time scale on which the meridional transport of the PF responds to the wind stress.

The meridional movement of φ_{PF} may simply correspond to meridional shifts in the wind field (φ_τ). For example, a northward shift of the maximum zonal wind stress may also force the Antarctic PF to move to the north. Here, both φ_{PF} and φ_τ have red spectra, and we prewhiten both records by using their derivatives. The coherence analysis of $\partial\varphi_{\text{PF}}/\partial t$ and $\partial\varphi_\tau/\partial t$ shows that in over 64% of the frequency domain, the coherence exceeds the 95% significance level, and the phase lag peaks at negative 10° (Fig. 12). This suggests that the PF location responds to shifts in the wind field ($\partial\varphi_{\text{PF}}/\partial t \propto \partial\varphi_\tau/\partial t$), with variations in the wind field leading variations in the PF.

Whether the Sverdrup balance holds in the ACC has also been the subject of much debate (Stommel 1957; Warren et al. 1996; Gnanadesikan and Hallberg 2000; Gent et al. 2001). Again, we examine the Sverdrup bal-

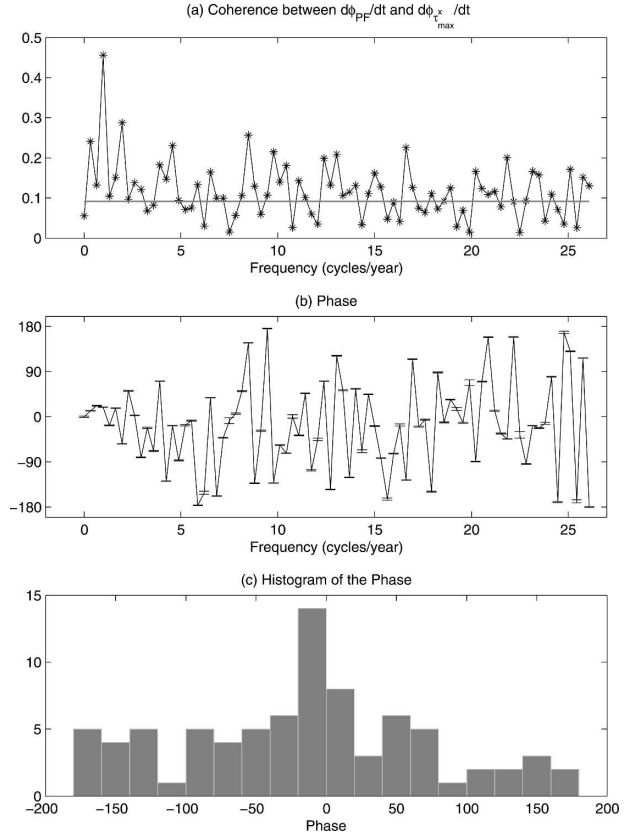


FIG. 12. (a) Coherence between the time derivative of the PF location and the time derivative of the location of the maximum zonal wind stress (95% significance level given by the gray line) and (b) the corresponding phase. (c) Histogram of the phase.

ance ($\beta V = \nabla \times \tau$) in a statistical sense using coherence analysis. Although the coherence between the wind stress curl and the Antarctic PF displacement in the meridional direction exceeds the 95% significance level at over 60% of the frequencies, no consistent phase relationship is found. This suggests that the Sverdrup balance does not hold, at least in our analysis. Our analysis shows that the location and the SST gradient of the PF and their time derivatives all show high coherence with the wind stress and wind stress curl at the annual frequency. However, without a more accurate estimate of the meridional transport and further analysis of the vorticity balance, we cannot conclude that the Sverdrup balance holds or that wind stress forces the transport of the PF on the seasonal time scale. The observed coherence may simply be due to the coincidence of the seasonal cycle in both fields.

5. Conclusions

The Antarctic PF location and its variability have been determined using 3 yr (June 2002–June 2005) of

SST measurements from the AMSR-E. The main advantage of the AMSR-E is that it provides all-weather SST measurements, though with lower spatial resolution than more traditional infrared SSTs. The PF is associated with a strong SST gradient, which is used to determine its location in this study. We define the PF as the southernmost location of the SST gradient above $1.5 \times 10^{-2}^{\circ}\text{C km}^{-1}$. The surface PF from our technique compares well with the subsurface PF determined from XBT temperatures, which suggests that our method is sensible. Consistent with previous studies, our results indicate that the surface PF location tends to be south of the subsurface PF location.

The mean PF path from AMSR-E is comparable with those from previous studies that use different datasets, especially over regions with steeply sloped bottom topography where the topographic constraint is strong. Bottom topography also plays an important role in the variability of the PF location and the SST gradient at the front. Over deep ocean basin regions with weak topographic variations, the PF meanders substantially, and the SST gradient is weak (Moore et al. 1999a; this study).

Both the PF location and SST at the PF show variations with longitude. The PF has a more southerly position and low temperature over the South Pacific section. In contrast, over the Atlantic and Indian Oceans, the PF has a more northerly position and higher temperature. The spatial distribution of the anomalous PF location does not show a zonally coherent seasonal cycle. The zonally averaged SST at the PF is dominated by seasonal variation. Unlike the PF path itself, the seasonal cycle of the SST at the PF is spatially coherent.

We have examined the statistical relationship of the wind field with the Antarctic PF location and with proxies for the zonal and meridional PF transports, represented by the SST gradient at the PF ($u \sim \partial T/\partial y$) and the time derivative of the PF location ($v \sim \partial \varphi_{\text{PF}}/\partial t$), respectively. Coherence analysis shows that the tendency of the SST gradient at the PF corresponds to the zonal wind stress: an enhancement of the SST gradient corresponds to a stronger zonal wind stress. This suggests that the zonal wind stress may play a role in the variability of the zonal PF transport. Our analysis also suggests a correspondence between the tendency of the PF location and the meridional shift of the wind field.

Acknowledgments. The authors thank Dr. Keith Moore and Dr. Igor Belkin for providing their mean PF paths. Special thanks are given also to Dr. Moore and an anonymous reviewer for helpful comments and suggestions. This study is supported by NASA Grant EOS/03-0602-0117 and NSF Grant OPP03-37998. STG ac-

knowledges support from NASA JPL Contracts 1222984 and 1224031.

REFERENCES

- Baker, D. J., 1982: A note on Sverdrup balance in the Southern Ocean. *J. Mar. Res.*, **40** (Suppl.), 21–26.
- Barcilon, V., 1967: Further investigation of the influence of the peripheral Antarctic water discharge on the Circumpolar Current. *J. Mar. Res.*, **25**, 1–9.
- Barth, J., A. T. J. Cowles, and S. D. Pierce, 2001: Mesoscale physical and biooptical structure of the Antarctic polar front near 170°W during austral spring. *J. Geophys. Res.*, **106**, 13 879–13 902.
- Belkin, I. M., and A. L. Gordon, 1996: Southern Ocean fronts from the Greenwich meridian to Tasmania. *J. Geophys. Res.*, **101**, 3675–3696.
- Botnikov, V. N., 1963: Geographic position of the Antarctic convergence zone in the Southern Ocean (English translation). *Sov. Antarct. Exped. Inf. Bull.*, **4**, 324–327.
- Boyd, P. W., C. Robinson, G. Savidge, P. J. Williams, and B. Le, 1995: Water column and sea ice primary production during austral spring in the Bellingshausen Sea. *Deep-Sea Res. II*, **42**, 1177–1200.
- Chelton, D. B., M. G. Schlax, D. L. Witter, and J. G. Richman, 1990: *Geosat* altimeter observations of the surface circulation of the Southern Ocean. *J. Geophys. Res.*, **95**, 17 877–17 903.
- Deacon, G. E. R., 1937: *The Hydrology of the Southern Ocean*. Discovery Reports, Vol. XV, Macmillan, 124 pp.
- Dong, S., S. T. Gille, J. Sprintall, and C. Gentemann, 2006: Validation of the Advanced Microwave Scanning Radiometer for the Earth Observing System (AMSR-E) sea surface temperature in the Southern Ocean. *J. Geophys. Res.*, **111**, C04002, DOI:10.1029/2005JC002934.
- Emery, W. J., and R. E. Thomson, 2001: *Data Analysis Methods in Physical Oceanography*. 2d ed. Elsevier Science, 638 pp.
- Ferry, N., G. Reverdin, and A. Oschlies, 2000: Seasonal sea surface height variability in the North Atlantic Ocean. *J. Geophys. Res.*, **105**, 6307–6326.
- Fofonoff, N. P., 1955: A theoretical study of zonally uniform oceanic flow. Ph.D. thesis, Brown University, 46 pp.
- Gent, P. R., W. G. Large, and F. Bryan, 2001: What sets the mean transport through Drake Passage? *J. Geophys. Res.*, **106**, 2693–2712.
- Gille, S. T., 1994: Mean sea surface height of the Antarctic Circumpolar Current from *Geosat* data: Method and application. *J. Geophys. Res.*, **99**, 18 255–18 273.
- , 1999: Mass, heat, and salt transport in the southeastern Pacific: A Circumpolar Current inverse model. *J. Geophys. Res.*, **104**, 5191–5210.
- , D. P. Stevens, R. T. Tokmakian, and K. J. Heywood, 2001: Antarctic Circumpolar Current response to zonally averaged winds. *J. Geophys. Res.*, **106**, 2743–2759.
- Gnanadesikan, A., and R. W. Hallberg, 2000: On the relationship of the Circumpolar Current to Southern Hemisphere winds in coarse-resolution ocean models. *J. Phys. Oceanogr.*, **30**, 2013–2034.
- Gordon, A. L., E. Molinelli, and T. N. Baker, 1978: Large-scale relative dynamic topography of the Southern Ocean. *J. Geophys. Res.*, **83**, 3023–3032.
- Hidaka, K., and M. Tsuchiya, 1953: On the Antarctic Circumpolar Current. *J. Mar. Res.*, **12**, 214–222.

- Holliday, N. P., and J. F. Read, 1997: Surface oceanic fronts between Africa and Antarctica. *Deep-Sea Res. I*, **45**, 217–238.
- Hughes, C. W., and E. R. Ash, 2001: Eddy forcing of the mean flow in the Southern Ocean. *J. Geophys. Res.*, **106**, 2713–2722.
- , M. P. Meredith, and K. J. Heywood, 1999: Wind-driven transport fluctuations through Drake Passage: A southern mode. *J. Phys. Oceanogr.*, **29**, 1971–1992.
- Johnson, G. C., and H. Bryden, 1989: On the strength of the Circumpolar Current. *Deep-Sea Res.*, **36**, 39–53.
- Lutjeharms, J. R. E., and H. R. Valentine, 1984: Southern Ocean thermal fronts south of Africa. *Deep-Sea Res.*, **31A**, 1461–1475.
- Moore, J. K., and M. R. Abbott, 2000: Phytoplankton chlorophyll distributions and primary production in the Southern Ocean. *J. Geophys. Res.*, **105**, 28 709–28 722.
- , —, 2002: Surface chlorophyll concentrations in relation to the Antarctic polar front: Seasonal and spatial patterns from satellite observations. *J. Mar. Syst.*, **37**, 69–86.
- , —, and J. G. Richman, 1997: Variability in the location of the Antarctic polar front (90° – 20° W) from satellite sea surface temperature data. *J. Geophys. Res.*, **102**, 27 825–27 833.
- , —, and —, 1999a: Location and dynamics of the Antarctic polar front from satellite sea surface temperature data. *J. Geophys. Res.*, **104**, 3059–3073.
- , —, —, W. O. Smith, T. J. Cowles, K. H. Coale, W. D. Gardner, and R. T. Barber, 1999b: SeaWiFS satellite ocean color data from the Southern Ocean. *Geophys. Res. Lett.*, **26**, 1465–1468.
- Morrow, R., A. Brut, and A. Chaigneau, 2003: Seasonal and interannual variations of the upper ocean energetics between Tasmania and Antarctica. *Deep-Sea Res. I*, **50**, 339–356.
- Munk, W. H., and E. Palmén, 1951: Note on the dynamics of the Antarctic Circumpolar Current. *Tellus*, **3**, 53–55.
- Nowlin, W. D., Jr., T. Whitworth III, and R. D. Pillsbury, 1977: Structure and transport of the Antarctic Circumpolar Current at Drake Passage from short-term measurements. *J. Phys. Oceanogr.*, **7**, 778–802.
- O'Neill, L. W., D. B. Chelton, and S. K. Esbensen, 2003: Observations of SST-induced perturbations of the wind stress field over the Southern Ocean on seasonal time scales. *J. Climate*, **16**, 2340–2354.
- , —, —, and F. J. Wentz, 2005: High-resolution satellite measurements of the atmospheric boundary layer response to SST variations along the Agulhas Return Current. *J. Climate*, **18**, 2706–2726.
- Orsi, A. H., T. Whitworth III, and W. D. Nowlin Jr., 1995: On the meridional extent and fronts of the Antarctic Circumpolar Current. *Deep-Sea Res. I*, **42**, 641–673.
- Park, Y. H., L. Gamberoni, and E. Charriaud, 1993: Frontal structure, water masses, and circulation in the Crozet Basin. *J. Geophys. Res.*, **98**, 12 361–12 385.
- Pegion, P. J., M. A. Bourassa, D. M. Legler, and J. J. O'Brien, 2000: Objectively derived daily “winds” from satellite scatterometer data. *Mon. Wea. Rev.*, **128**, 3150–3168.
- Peterson, R. G., 1988: On the transport of the Antarctic Circumpolar Current through Drake Passage and its relation to wind. *J. Geophys. Res.*, **93**, 13 993–14 004.
- Pollard, R. T., J. F. Read, J. T. Allen, G. Griffiths, and A. I. Morrison, 1995: On the physical structure of a front in the Bellingshausen Sea. *Deep-Sea Res. II*, **42**, 955–982.
- , M. I. Lucas, and J. F. Read, 2002: Physical controls on biogeochemical zonation in the Southern Ocean. *Deep-Sea Res. II*, **49**, 3289–3305.
- Read, J. F., R. T. Pollard, A. I. Morrison, and C. Symon, 1995: On the southerly extent of the Antarctic Circumpolar Current in the southeast Pacific. *Deep-Sea Res. II*, **42**, 933–954.
- Rintoul, S. R., J. R. Donguy, and D. H. Roemmich, 1997: Seasonal evolution of upper ocean thermal structure between Tasmania and Antarctica. *Deep-Sea Res. I*, **44**, 1185–1202.
- Sievers, H. A., and W. D. Nowlin Jr., 1984: The stratification and water masses at Drake Passage. *J. Geophys. Res.*, **89**, 10 489–10 514.
- Sokolov, S., and S. R. Rintoul, 2002: Structure of Southern Ocean fronts at 140° E. *J. Mar. Syst.*, **37**, 151–184.
- Sparrow, M. D., K. J. Heywood, J. Brown, and D. P. Stevens, 1996: Current structure of the south Indian Ocean. *J. Geophys. Res.*, **101**, 6377–6391.
- Sprintall, J., 2003: Seasonal to interannual upper-ocean variability in the Drake Passage. *J. Mar. Res.*, **61**, 27–57.
- Stommel, H., 1957: A survey of ocean current theory. *Deep-Sea Res.*, **6**, 149–184.
- Straub, D., 1993: On the transport and angular momentum balance of channel models of the Antarctic Circumpolar Current. *J. Phys. Oceanogr.*, **23**, 776–782.
- Sun, C., and D. R. Watts, 2002: Heat flux carried by the Antarctic Circumpolar Current mean flow. *J. Geophys. Res.*, **107**, 3119, doi:10.1029/2001JC001187.
- Tansley, C. E., and D. P. Marshall, 2001: On the dynamics of wind-driven circumpolar currents. *J. Phys. Oceanogr.*, **31**, 3258–3273.
- Warren, B., J. LaCase, and P. A. Robbins, 1996: On the obscurantist physics of “form drag” in theorizing about the circumpolar current. *J. Phys. Oceanogr.*, **26**, 2297–2301.
- Wearn, R. B., and D. J. Baker, 1980: Bottom pressure measurements across the Antarctic Circumpolar Current and their relation to the wind. *Deep-Sea Res.*, **27A**, 875–888.
- White, B. W., and C. Tai, 1995: Inferring interannual changes in global upper ocean heat storage from TOPEX altimetry. *J. Geophys. Res.*, **100**, 24 934–24 954.
- Yelland, M., and P. K. Taylor, 1996: Wind stress measurements from the open ocean. *J. Phys. Oceanogr.*, **26**, 541–558.